

# Lawrence Berkeley National Laboratory

## LBL Publications

### Title

Generation and control of nonlocal chiral currents in graphene superlattices by orbital Hall effect

### Permalink

<https://escholarship.org/uc/item/7w84j6ff>

### Journal

Physical Review Research, 6(2)

### ISSN

2643-1564

### Authors

Salvador-Sánchez, Juan

Canonico, Luis M

Pérez-Rodríguez, Ana

et al.

### Publication Date

2024-05-01

### DOI











10.1103/physrevresearch.6.023212

### Copyright Information

This work is made available under the terms of a Creative Commons Attribution License, available at <https://creativecommons.org/licenses/by/4.0/>

Peer reviewed

# Generation and control of nonlocal chiral currents in graphene superlattices by orbital Hall effect

Juan Salvador-Sánchez <sup>1</sup>, Luis M. Canonico <sup>2</sup>, Ana Pérez-Rodríguez,<sup>1</sup> Tarik P. Cysne <sup>3</sup>, Yuriko Baba,<sup>4</sup> Vito Clericò <sup>1</sup>,  
 Marc Vila,<sup>2,5,6</sup> Daniel Vaquero <sup>1</sup>, Juan Antonio Delgado-Notario <sup>1</sup>, José M. Caridad,<sup>1</sup> Kenji Watanabe <sup>7</sup>,  
 Takashi Taniguchi,<sup>8</sup> Rafael A. Molina <sup>9</sup>, Francisco Domínguez-Adame <sup>4</sup>, Stephan Roche,<sup>2,10</sup> Enrique Diez,<sup>1</sup>  
 Tatiana G. Rappoport,<sup>11,12,\*</sup> and Mario Amado <sup>1,†</sup>

<sup>1</sup>Nanotechnology Group, USAL—Nanolab, *University of Salamanca*, Plaza de la Merced, Edificio Trilingüe, 37008 Salamanca, Spain

<sup>2</sup>Catalan Institute of Nanoscience and Nanotechnology, CSIC and BIST, Campus UAB, Bellaterra, 08193 Barcelona, Spain

<sup>3</sup>Instituto de Física, *Universidade Federal Fluminense*, 24210-346 Niterói RJ, Brazil

<sup>4</sup>GISC, Departamento de Física de Materiales, *Universidad Complutense*, 28040 Madrid, Spain

<sup>5</sup>Department of Physics, *University of California, Berkeley*, California 94720, USA

<sup>6</sup>Materials Sciences Division, *Lawrence Berkeley National Laboratory*, Berkeley, California 94720, USA

<sup>7</sup>Research Center for Functional Materials, *National Institute for Materials Science*, 1-1 Namiki, Tsukuba 305-0044, Japan

<sup>8</sup>International Center for Materials Nanoarchitectonics, *National Institute for Materials Science*, 1-1 Namiki, Tsukuba 305-0044, Japan

<sup>9</sup>Instituto de Estructura de la Materia, IEM-CSIC, E-28006 Madrid, Spain

<sup>10</sup>ICREA—Institució Catalana de Recerca i Estudis Avançats, 08010 Barcelona, Spain

<sup>11</sup>Physics Center of Minho and Porto Universities (CF-UM-UP), Braga, Portugal

<sup>12</sup>Instituto de Física, *Universidade Federal do Rio de Janeiro*, C.P. 68528, 21941-972 Rio de Janeiro RJ, Brazil



(Received 2 November 2023; revised 13 March 2024; accepted 3 May 2024; published 28 May 2024)

Graphene-based superlattices offer a unique materials playground to exploit and control a higher number of electronic degrees of freedom, such as charge, spin, or valley for disruptive technologies. Recently, orbital effects, emerging in multivalley band structures lacking inversion symmetry, have been discussed as possible mechanisms for developing *orbitronics*. Here, we report nonlocal transport measurements in small gap hBN/graphene/hBN moiré superlattices which reveal very strong magnetic field-induced chiral response which is stable up to sizable temperatures. The measured sign dependence of the nonlocal signal with respect to the magnetic field orientation clearly indicates the manifestation of emerging orbital magnetic moments. The interpretation of experimental data is well supported by numerical simulations, and the reported phenomenon stands as a formidable way of *in situ* manipulation of the transverse flow of orbital information that could enable the design of orbitronic devices.

DOI: [10.1103/PhysRevResearch.6.023212](https://doi.org/10.1103/PhysRevResearch.6.023212)

## I. INTRODUCTION

The electronic properties of graphene and other two-dimensional (2D) materials with a honeycomb lattice are dictated by the low-energy physics at two inequivalent  $K$  and  $K'$  valleys of the reciprocal space [1]. The large momentum separation between these valleys allows distinguishing valley quantum numbers that, likewise the spin degree of freedom, can be used to store and process information [2]. Moreover, the valleys in graphene possess opposite orbital magnetic moments of topological origin [3], that at  $K$  and  $K'$  are proportional to the inverse of the band gap. This results in giant Zeeman splittings upon interaction with weak external magnetic fields, lifting valley degeneracy [4,5].

In gapped graphene, the application of an electric field has been predicted to induce a flow of electrons, moving in opposite directions for different valleys, and thus giving rise to a valley Hall effect (VHE) [6,7] that could be detected by nonlocal transport measurements [6–11]. However, this is also accompanied by a transverse flow of magnetic moments. Consequently, the VHE can also be depicted as an orbital Hall effect (OHE) [12]. In this latter interpretation, the orbital magnetic moments are physical quantities equally well-defined in the *entire momentum space* and in real space [13]. They replace the valley quantum numbers, which depend on the existence of well-defined pockets [12]. It is common knowledge that there is a flow of magnetic moments in the VHE but the observable is not calculated. The OHE formulation resolves this issue and also treats, on the same footing, situations where  $k$  might be not a good quantum number or situations where the electron lives in an arbitrary point of the Brillouin zone.

In the case of twisted structures, for instance, one might have the situation where, because of the formation of minibands, the orbital magnetic moment can present considerable variation around the mini Brillouin zone, which can be accessible by small changes of the Fermi energy. In that case, the whole mini Brillouin zone needs to be taken into account

\*tgrappoport@gmail.com

†mario.amado@usal.es

Published by the American Physical Society under the terms of the [Creative Commons Attribution 4.0 International license](https://creativecommons.org/licenses/by/4.0/). Further distribution of this work must maintain attribution to the author(s) and the published article's title, journal citation, and DOI.

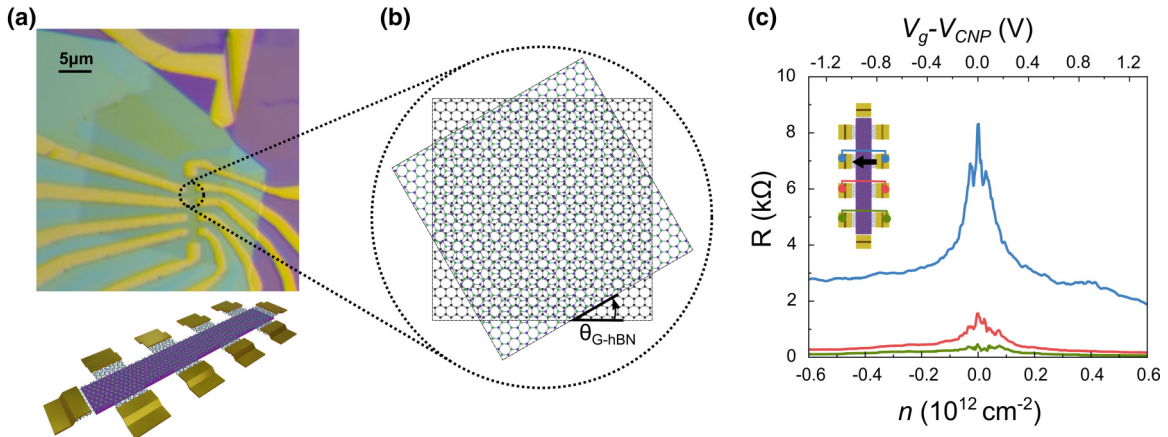


FIG. 1. (a) Optical image and schematics of a complete device, consisting of a heterostructure based on a graphite back gate (15 nm) and monolayer graphene encapsulated between two layers of hBN with thicknesses 10 nm (top) and 50 nm (bottom). (b) Art view schematic of a graphene/hBN heterostructure with a layer alignment set to  $\theta \approx 30^\circ$ . A moiré wavelength of  $\lambda \sim 0.47$  nm can be extracted from the relation found in Refs. [11,26], in stark contrast with the usual  $\lambda \sim 14$  nm present in fully aligned samples where  $\theta \approx 0^\circ$ . (c) Local and nonlocal resistances for the terminals indicated in the schematic representation of the final device, where the solid arrow serves as the direction of the driving (local) current as a function of the back-gate voltage in absence of external magnetic field. The two pairs of contacts are separated 2.5 and 5.0  $\mu\text{m}$  from the local signal.

for an accurate OHE calculation. From the bulk theory of the VHE in graphene, there is not a simple route to calculate, for example, the magnetic moment accumulation at the edges or even the possibility of having magnetic moments generated by band bending that can occur in real devices. Still, dispersive edge states can also give rise to orbital magnetic moments. This phenomenon was also reported for nanoribbons of kagome lattices, where the dispersive edge states of the systems are polarized in orbital momentum [14]. Thus, in sharp contrast with the VHE, the OHE refers to a transverse current of a physical observable that is naturally more general and also physically manipulable (i.e., magnetic field). Additionally, the OHE can also occur in disordered and finite systems, and can be used to analyze the interaction with magnetic and electric fields in the same framework.

The electronic structure of graphene-based van der Waals (vdW2Ds) heterostructures can be remarkably tailored by varying the twist angle between weakly interacting atomic layers to generate graphene moiré superlattices [6–8,10,11,15–17]. In this context, single or doubly aligned graphene/hexagonal boron nitride (hBN) heterojunctions are very interesting for the study of inversion symmetry breaking in graphene. Indeed, such systems present considerable nonlocality effect [8,10,18–20], whose origin, although frequently associated with the VHE, is strongly questioned [21–24]. Besides, it has been shown that doubly aligned hBN/graphene stacks might generate a supermoiré pattern [25], leading to the presence of small and nonuniform band gaps [23,24]. vdW2Ds are, henceforth, a perfect platform for the study of inversion symmetry breaking in graphene. Since the induced gaps are rather small, of the order of few meV, the valley orbital magnetic moments are large and can be manipulated with magnetic and electric fields.

In this paper, we report the unambiguous formation of chiral nonlocal currents in hBN/graphene/hBN heterostructures, presenting direct evidence of their orbital magnetic origin. Our alignment design between layers minimizes the band

gap, resulting in orbital magnetic moments of the order of  $10^2 \mu_B$ . The interaction with weak magnetic fields lifts their degeneracy, generating nonlocal chiral currents. Our quantum transport simulations in graphene nanoribbons with dispersive edge states and linear response theory calculations support our interpretation of the experimental findings regarding the origin of the chiral nonlocal resistance in graphene.

## II. RESULTS

Figure 1(a) displays an optical image of the heterostructure consisting of a graphite back gate (15 nm thick) and monolayer graphene encapsulated between a top and bottom layer of hBN with a thickness of 10 and 50 nm, respectively. The crystals were aligned following their exfoliated straight edges using a micromechanical rotator and, for that reason, the relative twisting angles along the vertical heterostructure, if perfectly aligned, are expected to obey  $m \times 30^\circ$ , being  $m = 0, \pm 1, \pm 2, \dots$ . From our electrical data displayed in Fig. S5 of the Supplemental Material [27], we can reasonably discard twisting angles between graphene and hBN that are fully aligned to  $0^\circ$  or a multiple of  $60^\circ$ . On the one side, the charge neutrality point (CNP) appears as a stand-alone main Dirac peak with no traces of secondary satellite peaks in the measured carrier density range  $|n| < 3 \times 10^{12} \text{ cm}^{-2}$  that arise from the existence of electron-hole pockets at both sides of the main peak at such twisting angles [10,11,15,17,18,20,28,29]. On the other side, CNP resistivity of heterostructures where graphene is aligned to  $0^\circ$  or  $60^\circ$  with the hBN exhibits a strong thermally activated behavior with values exceeding hundreds of  $\text{k}\Omega$  at low temperature, indicating a moiré coupling-induced band gap of the order of 30 meV [11,17,18,28,30]. In our case, we observe a thermally activated behavior at low temperature but a CNP resistivity of only  $\sim 7 \text{ k}\Omega$  at room temperature. These characteristics are consistent with band gaps smaller than 10 meV. Charge mobility extracted from

magnetotransport Hall measurements rises to  $220.000 \text{ cm}^2 \text{ Vs}$ , as shown in Fig. S5 of the Supplemental Material [27].

From a careful Raman analysis, we underpin the relative orientation of the flakes from the evolution of full width at half maximum of the 2D peak (FWHM2D) as a function of the twisting angle. Finney *et al.* [29] kept the bottom hBN aligned with graphene at  $0^\circ$  and varied the relative angle of the top layer from  $0^\circ$  to  $60^\circ$ . They showed that the vertical structure exhibits a noticeably high value of the FWHM2D, exceeding the standard one found in isolated graphene by 20 (40)  $\text{cm}^{-1}$  if one (both) hBN layer(s) is (are) aligned to the graphene at the commensurate angles of  $0^\circ$  or  $60^\circ$  [29]. Such broadening results from the moiré-scale relaxation of the graphene lattice, which strongly modifies the band structure [31]. We found a value of  $\sim 20 \text{ cm}^{-1}$  for the FWHM2D (see Fig. S4 in the Supplemental Material [27]), in good agreement with stand-alone graphene that would correspond to a twisting angle that is not aligned to neither  $0^\circ$  nor  $60^\circ$  [29]. The ratio between the 2D and G peaks  $I(2D)/I(G) > 9$  also strengthens the assumption of far-from-fully aligned layers with the most plausible scenario of twisting angles of  $\pm 30^\circ$  between graphene and hBN as presented in Fig. 1(b). In both cases, the system is expected to have a very small band gap as a consequence of the desired  $30^\circ$  desired misalignment between hBN and graphene, which will be of fundamental importance for the present paper.

Figure 1(c) shows the local ( $R_l$ ) and nonlocal resistances ( $R_{nl}$ ) for the pair of contacts indicated in the schematic view at 1.5 K. This allows us to infer the decay of the non-local signal as a function of the distance  $\Delta x_i$  between the injection (local, marked with a black arrow) and collection (nonlocal) terminals. For  $\Delta x_1 = 2.5 \mu\text{m}$  (nearest nonlocal contacts),  $R_{nl}$  takes a maximum value of  $\sim 1600 \Omega$  which is consistent with other nonlocal measurements in graphene/hBN heterostructures [8, 11, 18]. Moreover, the non-local signal gets weaker for increasing distances, reaching  $R_{nl} \sim 470 \Omega$  for  $\Delta x_2 = 5 \mu\text{m}$  (farthest non-local contacts). In the absence of external magnetic field, the position of the non-local peaks are aligned around the CNP and are symmetric with respect to electron/hole regions. The relation  $R_{nl}(\Delta x) = V_{nl}/I_0 \simeq \pi \rho_{xx} e^{-\pi|\Delta x|/W}$ , where  $W = 1.5 \mu\text{m}$  is the bar width, displays an exponential decay of the ohmic contribution to  $R_{nl}$  as a function of distance between the driving current and the nonlocal pair of contacts. This relation, already seen in graphene-based devices [18–20], serves to rule out the ohmic contribution to  $R_{nl}$  as its prevailing mechanism. We extracted the ratio between the measured nonlocal resistances at different distances, obtaining  $R_{nl}(\Delta x_2)/R_{nl}(\Delta x_1)|_{\text{Measured}} = 0.29$ , while the purely ohmic expression gives us  $R_{nl}(\Delta x_2)/R_{nl}(\Delta x_1)|_{\text{ohmic}} \sim 0.005$ . From this analysis, one can see that the nonlocal signal is orders of magnitude higher than the expected ohmic contribution (see Fig. S7 in the Supplemental Material [27]).

### III. CHIRAL NONLOCAL SIGNAL

To explore the relation between the nonlocal currents and orbital magnetic moments, we apply positive and negative perpendicular magnetic fields and analyze the nonlocal signals for different injection-collection configurations. Unless

stated otherwise, all measurements were performed at a fixed electronic temperature of 1.5 K and with an excitation current set to 10 – 20 nA. This low current amplitude was chosen to minimize thermal contributions to the nonlocal transport due to Joule heating and Ettingshausen effects [22] while simultaneously maximizing the signal-to-noise ratio of the measured voltages. A summary of our results is shown in Fig. 2, which contains nine different panels divided in three columns. Each column presents a different configuration of the external magnetic field, i.e.,  $-0.5 \text{ T}$ ,  $0 \text{ T}$ , and  $0.5 \text{ T}$ . Each of the three rows presents a different injection-collection setup, sketched in the diagram on the left. Each pair of contacts on the diagram has a specific color, while the arrows show the direction of the current for the pair of contacts of a particular injection-collection configuration. Each panel displays the local and nonlocal resistances as a function of the voltage applied to the graphite back gate. Their color palette matches the ones of the corresponding contacts, irrespective of the specific injection-collection setup.

Let us first comment on the effect of the magnetic field on the local resistances. The CNP is located at  $V_g \sim 0.6 \text{ V}$ , as extracted from the Lorentzian fit of the local resistance, and does not present a noticeable shift when the magnetic field is applied. Still, there is a sharp increase of the local resistance with the magnetic field, which is very pronounced at the CNP. Figure 2(b1) displays the evolution of the nonlocal signal as a function of the distance without external magnetic field. Figure 2(b2) represents a configuration of the nonlocal pairs of contacts that are placed symmetrically to the current flow but at opposite directions. In this case, the homogeneity of the sample is demonstrated because the nonlocal signals at both sides of the current flow have an expected matching value, as the magnitude of the nonlocal signal decays with the absolute value of the distance to the injection current. This characteristic, discussed previously, can also be seen in Figs. 2(a2) and 2(c2).

A striking behavior of the nonlocal signal arises in the presence of an external magnetic field. We first focus on the case where the current is injected between two nonlocal contacts. Figure 2(a2) shows the nonlocal resistances for the  $B = -0.5 \text{ T}$ , where one can see a clear separation between the peaks of opposite contacts. Moreover, they are mostly located either in the electron or hole sectors. Surprisingly, the position of the two peaks is swapped upon magnetic field reversal, which is a clear indication of a chiral behavior of the electronic response. If the two collectors are located at the same side of the injector, as shown in the first and last row of Fig. 2, the situation is different. In these two cases, the two nonlocal resistance peaks are aligned and located either at the electron or hole sector and switch positions with the sign of the magnetic field and the relative orientation with respect to the collector. While both peaks appear at the hole sector in Fig. 2(a1), when the sign of  $B$  is reversed, they appear at the electron sector [see Fig. 2(c1)]. If instead we switch the position for positive  $B$ , as in Fig. 2(a3), the peaks also appear at the electron sector, changing to the hole sector if the field is reversed [see Fig. 2(c3)]. It is worth mentioning the presence of reduced spurious peaks in Fig. 2, labeled as \*, and might arise from nonperfect carrier-valley locking in our results. These reduced nonlocal spurious peaks appear exactly

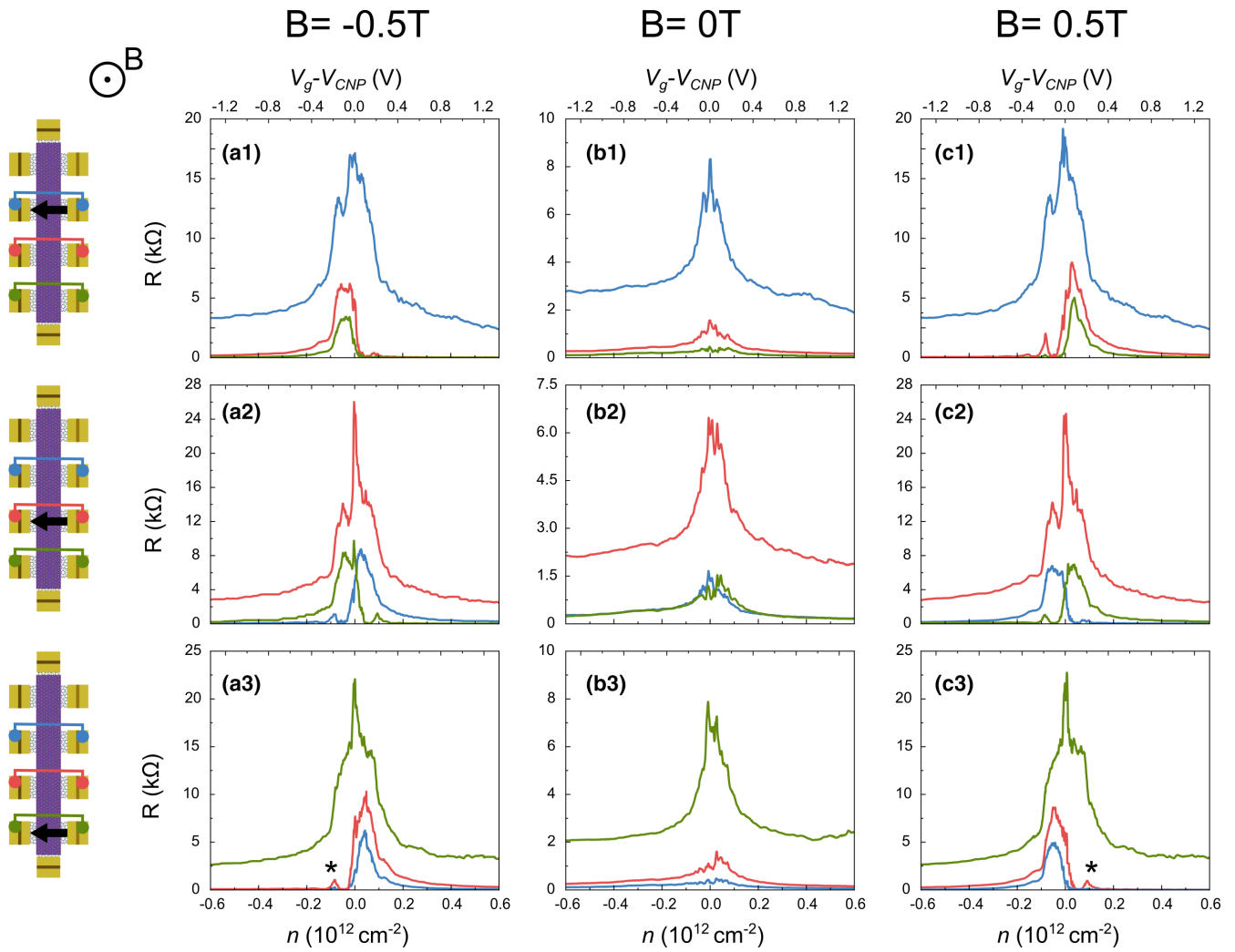


FIG. 2. Local and nonlocal resistances for three different (1–3) configurations of the injection-collection terminals in the transversal direction as a function of the back-gate voltage. The left column includes schematic top view of the corresponding configuration for each row of graphs where the local resistance will be measured across the pair of contacts connected by the driving current marked by the solid arrow. Each column corresponds to a different value of the magnetic field in the out-of-plane direction. The similarity of the nonlocal resistivity values in the absence of applied magnetic field shown in (b2) evidences the homogeneity and, in general, the good quality of the sample. Moreover, similar values arise for opposing configurations (as in rows 1 and 3) for opposite directions of the applied magnetic field, as can be observed comparing (a1) and (c3) with (a3) and (c1), for example. Peaks labeled by \* are ascribed to nonperfect carrier-valley locking within the whole sample, which can be attributed to a slight inhomogeneity in it. These peaks are nondominant and do not rule out the main findings presented in this paper.

at densities matching their dominant chiral counterparts and, while relevant, do not contradict our interpretation since they can be ascribed to nondominant imperfections in the final device arising from nonperfect valley-carrier locking within the whole sample. Furthermore, it is important to mention that in resemblance to similar experiments, the nonlocality is strongly enhanced with the magnetic field in all configurations [15,18,20].

The nine panels in Fig. 2 provide full demonstration of a chiral behavior of the nonlocal signal at low magnetic fields, which has not been reported in similar graphene-based heterostructures with twisting angles set to different commensurate angles [11,18,20]. In contrast to these works, the chiral response for the nonlocal signal cannot be attributed to electron-hole puddles or charge accumulation at the edges,

which should be symmetrical upon the application of external magnetic fields. Moreover, while band-bending mechanisms could provoke measurable nonlocal signals in these structures, it has already been demonstrated to be inhomogeneous [32], i.e., measurable for one kind of carrier and depleted for the other one and, therefore, it does not align to our findings either. To clarify the underlying mechanism, we use the modern theory of magnetism to address the effect of the fields in bulk calculations. Although the orbital magnetic moments of electrons in moiré heterostructures remain to be understood, their phenomenology can be tentatively related to the effective  $g$  factor of semiconductors, where the orbital motion of electrons can lead to enhanced magnetic responses [33]. The theoretical description [3,34,35] derives from treating Bloch electrons as self-rotating wave packets and

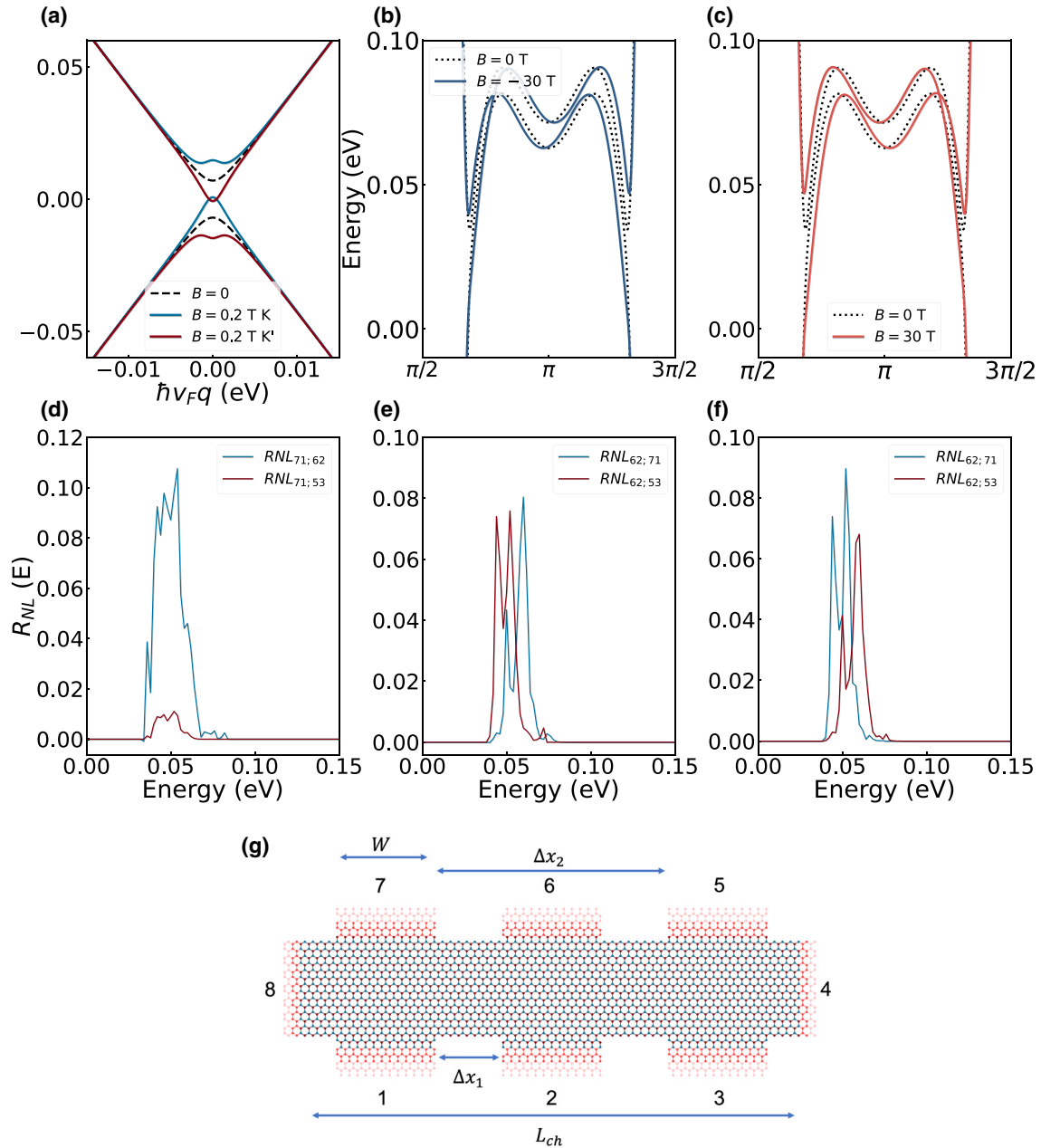


FIG. 3. (a) Comparison between the energy bands of gapped graphene systems with and without out-of-plane magnetic fields with  $B = 0.2$  T and a gap  $\Delta = 14$  meV. Comparison between the energy bands of zigzag graphene nanoribbons for  $B = 0$  and  $B = -30$  T (b) and  $B = +30$  T (c) with a sublattice staggered potential  $V_{ab} = 5$  meV. (d)–(f) Nonlocal resistance signals for lateral (d) and central (e), (f) current injection computed using 60 Anderson disorder realizations with  $U = V_{pp\pi}/128$  and  $V_{pp\pi} = -3.26$  eV, and sublattice staggered potential  $V_{ab} = 5$  meV, as a function of the energy for  $B = 0$  T,  $B = -30$  T and  $B = 30$  T, respectively. (g) Schematic representation of the device used in the simulations, with  $L_{ch} = 512$  nm,  $W = 13$  nm,  $\Delta x_1 = L_{ch}/3 - W$  and  $\Delta x_2 = 2L_{ch}/3 - W$ .

through the incorporation of the Berry phase theory to express the magnetic moment purely in terms of bulk quantities. Following Ref. [36], for gapped Dirac materials the orbital magnetic moment  $\mathbf{m}(\mathbf{k}) = (\tau e\hbar/2m^*)(1 + \hbar^2 v_F^2 k^2/\Delta^2)^{-1} \hat{\mathbf{z}}$ , where  $\tau = \pm 1$  is the valley quantum number,  $m^* = \Delta/v_F^2$  is the effective mass at the Dirac point (DP),  $\Delta$  is the system gap and  $v_F$  is the Fermi velocity. At the Dirac points, the orbital magnetic moment is inversely proportional to the gap width, while it can generally be seen as inversely proportional to the effective mass as well. Similarly to spins, this orbital moment

can couple directly with weak magnetic fields. This gives rise to a  $k$ -dependent Zeeman splitting that, in first-order perturbation theory, renormalizes the energy spectrum close to the Dirac points [36,37], as depicted in Fig. 3(a). As the valleys have opposite magnetic moments, the Zeeman effect produces a relative shift between the valleys. For small gaps, it can even lead to situations where the Fermi energy lies inside the gap for one valley while it is located in the electron (hole) sector for the other, as illustrated in Fig. 3(a). Given the coupling with the external fields, one can argue that the chiral behavior

observed in the nonlocal resistance appears as a manifestation of the Zeeman effect but with enhanced  $g$  factor of the order of 100, allowed by the formation of a small gap in the doubly encapsulated hBN/graphene/hBN heterostructure. The OHE interpretation is in fully agreement with the chiral behavior observed experimentally, shown in Fig. 2 (see details in the Supplemental Material [27]). The magnetic moments of each valley flow in opposite directions. Because of the sign of the Berry curvature, the flows invert directions when switching from hole to electron sectors. At the same time, the Zeeman shift between the valleys leads to a relative shift between the nonlocal peaks that should invert with the change in the magnetic field orientation and collector's locations. Using this reasoning, we can estimate the band gap from nonlocal peaks of Fig. 2(a2), obtaining  $\Delta \sim 5 - 8$  meV. One should mention that for this formulation, in general, the orbital angular momentum current is not conserved. Other approaches, useful for spin currents, allow alternative formulation of conserved currents of nonconserved quantities [38,39].

To validate our scenario, we further performed quantum transport simulations using the Landauer-Büttiker formalism implemented in KWANT [40]. In our calculations, we considered a multiterminal device containing a graphene nanoribbon geometry with contacts [Fig. 3(g)] in the presence of an external magnetic field. The advantage of this approach is that it does not rely on any assumption about the orbital Zeeman effect, as the magnetic field is included through the Peierls' substitution. Moreover, this geometry can connect directly with the experiments, as it considers contributions from the bulk and edge states and allows the calculation of nonlocal resistances. Still, here we are not particularly interested in the specific channels carrying the orbital currents. As will become clear below, the orbital Zeeman effect is present in bulk and edge states and either of them can, in principle, convey chiral nonlocal currents.

Previous numerical simulations showed the need for dispersive edge states near the Dirac point for nonlocal transport in gapped graphene [21]. They are absent in theories based on the simplistic Hamiltonian considering a single  $p_z$  orbital. Here, with full generality, we used a six-band tight-binding model that also takes into account the  $d$  orbitals [41] and a staggered sublattice potential to break the inversion symmetry of the system. It is important to note that other effects such as nonuniform potential and coupling to hBN layers can also lead to dispersive edge states and a similar nonlocal response (see details in the Supplemental Material [27]).

Figures 3(b) and 3(c) depicts the comparison between the energy bands of the nanoribbon with negative (positive) magnetic field and the energy states of the nanoribbon in the absence of magnetic field. The energy bands from this multiorbital model exhibit a dispersive behavior similar to the ones observed from *ab initio* calculations of Ref. [21]. It does not present a band gap, although there is a clear valence-conduction band separation due to the inversion symmetry breaking and very well-defined electron pockets at opposite sides of the nanoribbon Brillouin zone. The most relevant feature displayed by the two panels is the stark  $k$ -dependent coupling with the magnetic field, which is similar to the one observed in the bulk bands. Although the modern theory of magnetism is well developed only for bulk systems, it is clear,

from the results in panels 3(b) and 3(c), that the behavior displayed by the energy bands of the nanoribbon is in qualitative agreement with this theory.

Aiming to reproduce results from the middle columns in Fig. 2, in Figs. 3(d)–3(f) we used the same injection-collection scheme for our nonlocal resistance simulations. Figure 3(d) portrays the case in which the injection occurs at one side of the device in the absence of magnetic field. As in the measurements, the simulation results show considerable decay of the nonlocal signal with the channel length. However, the most striking behavior appears when we inject current in the middle contact of the device and calculate the nonlocal resistance at the two lateral contact pairs in the presence of an external magnetic field. Comparing these figures with the measurements shown in Fig. 2, we find convincing agreement between the chiral behavior displayed by the nonlocal resistance simulations in Figs. 3(e) and 3(f) with the measurements from Figs. 2(a2) and 2(c2), respectively. Moreover, the comparison between numerical results and the renormalized energy bands in Fig. 3 indicates that the mechanism at play in the generation of these nonlocal signals observed in the experiment is the orbital valley Hall effect [12]. The chirality and energy selectivity are directly related to the coupling between the orbital magnetic moment and the external magnetic field. Still, our analysis suggests that Fermi surface edge currents carry the nonlocal signal once the absence of dispersive edge states destroys the nonlocal signal.

Figures 4(b) and 4(c) display the contour plot of  $R_{nl}$  as a function of both  $B$  and  $V_g - V_{DP}$  for two symmetrical configurations for the local and nonlocal contacts as sketched in Fig. 4(a). The electronic temperature at which the curves were recorded was  $T = 250$  mK and the voltage has been centered at the Dirac peak for  $B = 0$ . Panels 4(b) and 4(c) show a clear chiral behavior and an apparent valley-carrier locking in the nonlocal signal for low magnetic fields ranging from  $-0.5$  to  $0.5$  T. In Fig. 4(b), we can observe a distinct transition from an electron-mediated nonlocal transport for negative magnetic fields towards a holelike one when the magnetic field is reversed. Moreover, a strong asymmetry in the nonlocal curves is clearly visible, with a sudden decay while approaching the DP from the dominant carrier species towards the prohibited one. Figure 4(c) displays the mirrored configuration for the pairs of contacts, compared to Fig. 4(b) as sketched in Fig. 4(a). Consequently, we can argue that the valley-carrier locking, visible in the nonlocal signal, is a quite robust phenomenon and implies a flow of carriers characterized by different orbital magnetic moments. As the nonlocal signal should originate from the flow of orbital magnetic moments from a single valley, we compare  $R_{nl}$  with the valley-filtered OHE, calculated according to Ref. [12], shown in the Figs. 4(d) and 4(e). To confirm this hypothesis, we also compare the measured shift in the maximum of the nonlocal resistance signals in neighboring contacts for various magnetic fields and opposite injection-detection configurations for sample 1. The agreement between the OHE for gaps of 8 meV and the measured shift up to  $\pm 0.5$  T, where the low-energy theory remains valid, is very convincing (see details in the Supplemental Material [27]). Consequently, the interpretation of the experimental results is fully consistent with the changes in the OHE resulting from the orbital Zeeman effect.

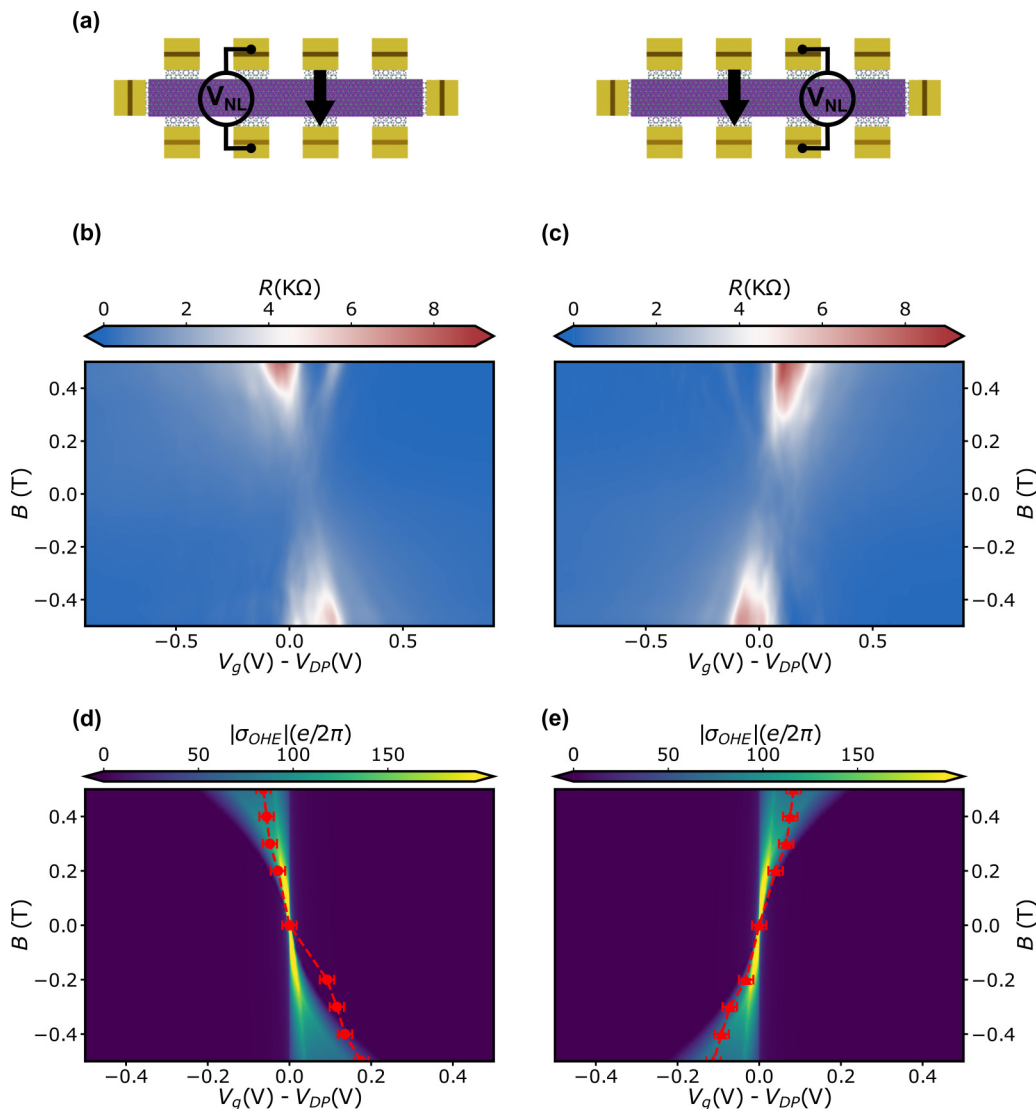


FIG. 4. (a) Sketch for the two different injection and collection configurations for the experimental and theoretical results shown in (b) and (c). (b), (c) Heat maps of the sample nonlocal resistance for two symmetrical configurations scanned in the space of back-gate voltage, corrected by the position of the Dirac peak at  $B = 0$  ( $V_G - V_{DP}$ ), and magnetic field measured at 250 mK. (d), (e) Numerical results for the OHE conductivity using Eq. (S8) in the Supplemental Material [27] for an energy gap  $\Delta = 8$  meV; the red markers correspond to the measured peak in the nonlocal signal as a function of the parameters, showing extraordinary agreement with the experimental results.

Importantly, the origin of the nonlocal resistance signals could also be related to some spin-dependent effect, which can be typically probed by applying in-plane magnetic fields and producing field-driven oscillations of non-local resistance. To discard such effect, we performed local and nonlocal measurements for a configuration where the excitation current lies symmetrically between two different pairs of contacts for  $R_{nl}$  at a fixed perpendicular magnetic field of  $B_{\perp} = 0.5$  T and for varying in-plane component ( $B_{\parallel}$ ) measured at 1.5 K (see Fig. 5).  $B_{\parallel}$  ranges from 0 to 12 T and its evolution have been marked with an arrow as a guide to the eye in the three different panels (a)–(c). For  $B_{\parallel} = 0$ , the charge carrier type is effectively coupled to one of the valleys and the asymmetric chiral behavior is clearly seen (see Fig. 5). In contrast, the increase of  $B_{\parallel}$  reduces the intensity of the nonlocal and local signals, which additionally becomes symmetric. From these

data, it becomes clear that spin-dependent effect cannot explain the measured chiral nonlocal currents.

On the other hand, in-plane magnetic fields can actually be used as a tuning parameter to manipulate the orbital characteristics of 2D multilayers and twisted bilayers and moiré superlattices [42,43].  $B_{\parallel}$  affects the quasimomentum of each layer differently [44–47], modifying the effective coupling between the layers and thus the resulting band structure. Indeed,  $B_{\parallel}$  introduces a layer-dependent gauge field  $\mathbf{A}_l = \mathbf{B}_{\parallel} \times \mathbf{z}_l$  that modifies the electron momentum  $\mathbf{p} \rightarrow \mathbf{p} + (e/c)\mathbf{A}_l$ , where  $l$  indexes the layer. For graphene encapsulated by two hBN layers and located at  $z = 0$ , the magnetic field shifts the momenta of electrons in each hBN layer along opposite directions. In addition, since time-reversal symmetry is broken, the momenta of the electrons of different valleys are shifted in the same direction, altering the band structure and the resulting



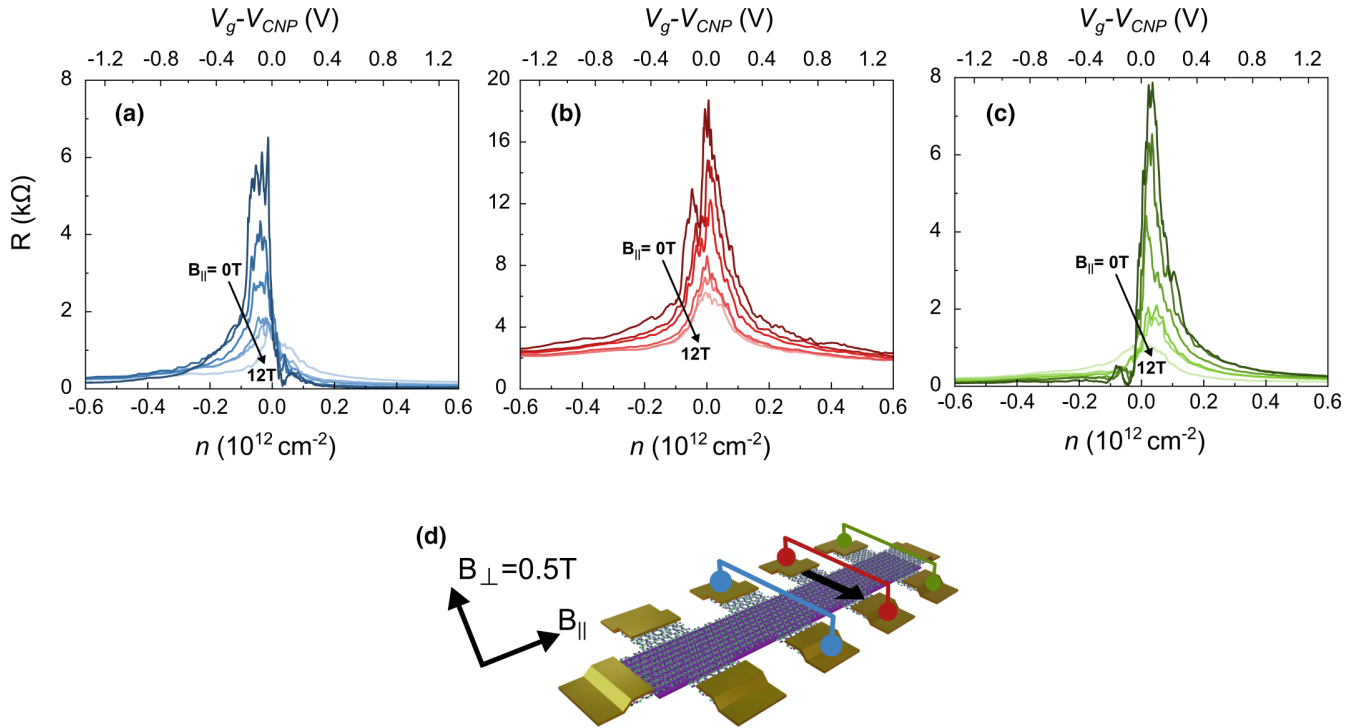


FIG. 5. Evolution of the nonlocal [(a), (c)] and local [(b)] resistances as a function of the external in-plane magnetic field for a fixed out-of-plane field  $B_{\perp} = 0.5$  T. Panel (d) sketches the sample, showing the direction of the driving current, the two pairs of contacts for nonlocal measurements, and the two components for the external magnetic field. Solid arrows show the evolution of the in-plane component for  $B$  ranging from 0 to 12 T.

orbital magnetic moments with a direct impact on local and nonlocal signals.

In conclusion, we have presented nonlocal transport measurements on hBN/graphene/hBN narrow gap heterostructures at low magnetic fields, which clearly indicate the presence of chiral effects. Such chiral response is inferred from the nonlocal resistance when reversing both the magnetic field and the injection-collection configurations. The interaction between large orbital magnetic moments arising in small gap graphene-based superlattices and external magnetic field produces a relative Zeeman shift between the two valleys in both bulk and edge electron states. Furthermore, based on our experimental and theoretical analysis, regardless of the details about the location of the current flow, the manifestation of a strong chiral effect originates from the interplay between the Zeeman shift and the transverse flow of orbital magnetic moments. Importantly, the analysis of the nonlocal transport as a function of the magnetic field direction rules out spin effects, whereas its dependence on the distance between contacts clarifies that ohmic and thermal contributions are marginal. Finally, our computational results show that the orbital valley Hall effect displays fingerprints in both bulk and edge transport, being of topological nature or not. All these facts convincingly support the interpretation that the origin of the giant nonlocality in the studied graphene superlattices is linked to the OHE resulting from the valley magnetic moments. Beyond shining light on a fierce debate concerning the formation of topological versus nontopological valley-driven phenomena to explain previously reported nonlocal signals

[24,48], our findings pave the way towards future developments in graphene orbitronics.

#### IV. METHODS

The device fabrication of the superlattices follows the standard dry transfer technique with a polycarbonate film fabricated and deposited onto a polydimethylsiloxane stamp. The relative rotation between the different layers, following their natural edges, was controlled using a heated stage with a micromechanical rotator with an accuracy better than  $0.5^{\circ}$ . The heterostructure rested atop a commercial Si/SiO<sub>2</sub> substrate. The fabricated stack was patterned using electron beam lithography followed by a dry-etching process in an ICP-RIE to define the sample geometry. The sample was patterned into a form of a multiterminal Hall bar (optical image in Fig. 1) with the central horizontal bar of width  $W = 1.5 \mu\text{m}$ , total length of  $\sim 11 \mu\text{m}$ , and a distance between the centers of the contacts of  $2.5 \mu\text{m}$ . Electrical contact to all devices was made by Cr/Au (10 nm/50 nm) deposited by electron beam evaporation (see Fig. S1 and S2 in the Supplemental Material [27]). We extracted the all Raman spectra and their associated FWHM2D from a Lorentzian fit (see details in the Supplemental Material [27]). Transport measurements in the multiterminal device were conducted in two- and four-terminal geometries with ac current excitation of 10-20 nA using the standard lock-in technique at 17.7 Hz. The graphite layer was gated by applying a direct bias to it in the range of  $\pm 12$  V.

All data needed to evaluate the findings of this study are present in the paper and/or the Supplemental Material. Data are available from the corresponding authors on reasonable request.

### ACKNOWLEDGMENTS

M.A. and E.D. acknowledge financial support from the Ministerio de Ciencia e Innovación of Spain (Spanish Ministry of Science, Innovation, and Universities) and FEDER (ERDF: European Regional Development Fund) under Research Grants No. PID2019-106820RB-C21/22, No. PID2022-136285NB-C32, and FEDER/Junta de Castilla y León Research Grant No. SA121P20. A.P.-R. acknowledges financial support received from the Marie Skłodowska Curie-COFUND program under the Horizon 2020 research and innovation initiative of the European Union, within the framework of the USAL4Excellence program (Grant Agreement No. 101034371). D.V. acknowledges financial support from the Ministerio de Universidades (Spain) (Ph.D. Contract No. FPU19/04224), including funding from ERDF/FEDER. J.S.-S. acknowledges financial support from the Consejería de Educación, Junta de Castilla y León, and ERDF/FEDER. L.M.C. acknowledges funding from MCIU/AEI/10.13039/501100011033 and European Union NextGenerationEU/PRTR under Grant No. FJC2021-047300-I. S.R. acknowledges funding from the European Union Seventh Framework Programme under Grant No. 881603 (Graphene Flagship). The Catalan Institute of Nanoscience and Nanotechnology (ICN2) is funded by the CERCA Programme/Generalitat de Catalunya and supported by the Severo Ochoa programme (MINECO Grant No. SEV-2017-0706. S.R. is also supported by MCIU with European funds-NextGenerationEU 324 (PRTR-C17.I1) and by Generalitat de Catalunya. T.G.R. acknowledges funding from FCT-Portugal

through Grant No. 2022.07471.CEECIND/CP1718/CT0001 [63] and in the framework of the Strategic Funding UIDB/04650/2020. T.P.C. acknowledges financial support from Brazilian agency CAPES. J.M.C. acknowledges support from the MICINN Ramón y Cajal program (Project No. RYC2019-028443-I). M.V. was supported as part of the Center for Novel Pathways to Quantum Coherence in Materials, an Energy Frontier Research Center funded by the U.S. Department of Energy, Office of Science, Basic Energy Sciences. K.W. and T.T. acknowledge support from JSPS KAKENHI (Grants No. 19H05790, No. 20H00354, and No. 21H05233). J.A.D.-N. acknowledges support from Junta de Castilla y León cofunded by FEDER under Research Grant No. SA103P23 and the support from the Universidad de Salamanca for the María Zambrano postdoctoral grant funded by the Next Generation EU Funding for the Requalification of the Spanish University System 2021–23, Spanish Ministry of Universities. F.D.-A. and Y.B. were supported by the Recovery, Transformation and Resilience Plan, funded by the European Union NextGenerationEU (Grant No. MAD2D-CM-UCM5) and Ministerio de Ciencia e Innovación of Spain (Grant No. PID2022-136285NB-C31).

M.A., E.D. and F.D.-A. developed the concept of the experiment. T.T. and K.W. provided hBN crystals. J.S.-S., A.P.-R., V.C., D.V., and J.A.D.-N. performed device fabrication and carried out Raman spectroscopy. J.S.-S., A.P.-R.E.D., and M.A. performed transport measurements. J.S.-S. and A.P.-R. performed experimental analysis. J.S.-S., A.P.-R., E.D., and M.A. interpreted results with help from L.M.C., T.G.R., S.R., J.M.C., Y.B., R.A.M., and F.D.-A. Theoretical calculations were performed by L.M.C., T.G.R., T.P.C., M.V., and S.R. The paper and the Supplemental Material were written by T.G.R., M.A., S.R., L.M.C., J.S.-S., A.P.-R., and F. D.-A., with additional contributions from all authors.

The authors declare that they have no competing interests.

- 
- [1] A. H. C. Neto, F. Guinea, N. M. R. Peres, K. S. Novoselov, and A. K. Geim, The electronic properties of graphene, *Rev. Mod. Phys.* **81**, 109 (2009).
- [2] D. Xiao, W. Yao, and Q. Niu, Valley-contrasting physics in graphene: Magnetic moment and topological transport, *Phys. Rev. Lett.* **99**, 236809 (2007).
- [3] D. Xiao, M.-C. Chang, and Q. Niu, Berry phase effects on electronic properties, *Rev. Mod. Phys.* **82**, 1959 (2010).
- [4] Z. Ge, S. Slizovskiy, F. Joucken, E. A. Quezada, T. Taniguchi, K. Watanabe, V. I. Fal'ko, and J. Velasco, Control of giant topological magnetic moment and valley splitting in trilayer graphene, *Phys. Rev. Lett.* **127**, 136402 (2021).
- [5] J. Yin, C. Tan, D. Barcons-Ruiz, I. Torre, K. Watanabe, T. Taniguchi, J. C. W. Song, J. Hone, and F. H. L. Koppens, Tunable and giant valley-selective Hall effect in gapped bilayer graphene, *Science* **375**, 1398 (2022).
- [6] M. Sui, G. Chen, L. Ma, W.-Y. Shan, D. Tian, K. Watanabe, T. Taniguchi, X. Jin, W. Yao, D. Xiao, and Y. Zhang, Gate-tunable topological valley transport in bilayer graphene, *Nat. Phys.* **11**, 1027 (2015).
- [7] M. J. Zhu, A. V. Kretinin, M. D. Thompson, D. A. Bandurin, S. Hu, G. L. Yu, J. Birkbeck, A. Mishchenko, I. J. Vera-Marun, K. Watanabe, T. Taniguchi, M. Polini, J. R. Prance, K. S. Novoselov, A. K. Geim, and M. B. Shalom, Edge currents shunt the insulating bulk in gapped graphene, *Nat. Commun.* **8**, 14552 (2017).
- [8] R. V. Gorbachev, J. C. W. Song, G. L. Yu, A. V. Kretinin, F. Withers, Y. Cao, A. Mishchenko, I. V. Grigorieva, K. S. Novoselov, L. S. Levitov, and A. K. Geim, Detecting topological currents in graphene superlattices, *Science* **346**, 448 (2014).
- [9] Y. Shimazaki, M. Yamamoto, I. V. Borzenets, K. Watanabe, T. Taniguchi, and S. Tarucha, Generation and detection of pure valley current by electrically induced Berry curvature in bilayer graphene, *Nat. Phys.* **11**, 1032 (2015).
- [10] K. Komatsu, Y. Morita, E. Watanabe, D. Tsuya, K. Watanabe, T. Taniguchi, and S. Moriyama, Observation of the quantum valley Hall state in ballistic graphene superlattices, *Sci. Adv.* **4**, eaq0194 (2018).
- [11] Y. Li, M. Amado, T. Hyart, G. P. Mazur, and J. W. A. Robinson, Topological valley currents via ballistic edge modes in graphene

- superlattices near the primary Dirac point, *Commun. Phys.* **3**, 224 (2020).
- [12] S. Bhowal and G. Vignale, Orbital Hall effect as an alternative to valley Hall effect in gapped graphene, *Phys. Rev. B* **103**, 195309 (2021).
- [13] R. Bianco and R. Resta, Orbital magnetization in insulators: Bulk versus surface, *Phys. Rev. B* **93**, 174417 (2016).
- [14] O. Busch, I. Mertig, and B. Gobel, Orbital Hall effect and orbital edge states caused by  $s$  electrons, *Phys. Rev. Res.* **5**, 043052 (2023).
- [15] L. A. Ponomarenko, R. V. Gorbachev, G. L. Yu, D. C. Elias, R. Jalil, A. A. Patel, A. Mishchenko, A. S. Mayorov, C. R. Woods, J. R. Wallbank, M. Mucha-Kruczynski, B. A. Piot, M. Potemski, I. V. Grigorieva, K. S. Novoselov, F. Guinea, V. I. Fal'ko, and A. K. Geim, Cloning of Dirac fermions in graphene superlattices, *Nature (London)* **497**, 594 (2013).
- [16] C. R. Dean, L. Wang, P. Maher, C. Forsythe, F. Ghahari, Y. Gao, J. Katoch, M. Ishigami, P. Moon, M. Koshino, T. Taniguchi, K. Watanabe, K. L. Shepard, J. Hone, and P. Kim, Hofstadter's butterfly and the fractal quantum Hall effect in moiré superlattices, *Nature (London)* **497**, 598 (2013).
- [17] R. Ribeiro-Palau, C. Zhang, K. Watanabe, T. Taniguchi, J. Hone, and C. R. Dean, Twistable electronics with dynamically rotatable heterostructures, *Science* **361**, 690 (2018).
- [18] D. A. Abanin, S. V. Morozov, L. A. Ponomarenko, R. V. Gorbachev, A. S. Mayorov, M. I. Katsnelson, K. Watanabe, T. Taniguchi, K. S. Novoselov, L. S. Levitov, and A. K. Geim, Giant nonlocality near the Dirac point in graphene, *Science* **332**, 328 (2011).
- [19] M. Ribeiro, S. R. Power, S. Roche, L. E. Hueso, and F. Casanova, Scale-invariant large nonlocality in polycrystalline graphene, *Nat. Commun.* **8**, 2198 (2017).
- [20] A. Aharon-Steinberg, A. Marguerite, D. J. Perello, K. Bagani, T. Holder, Y. Myasoedov, L. S. Levitov, A. K. Geim, and E. Zeldov, Long-range nontopological edge currents in charge-neutral graphene, *Nature (London)* **593**, 528 (2021).
- [21] J. M. Marmolejo-Tejada, J. H. Garcia, M. D. Petrović, P. H. Chang, X. L. Sheng, A. Cresti, P. Plecháč, S. Roche, and B. K. Nikolić, Deciphering the origin of nonlocal resistance in multiterminal graphene on hexagonal-boron-nitride with *ab initio* quantum transport: Fermi surface edge currents rather than Fermi sea topological valley currents, *J. Phys. Mater.* **1**, 015006 (2018).
- [22] J. Renard, M. Studer, and J. A. Folk, Origins of nonlocality near the neutrality point in graphene, *Phys. Rev. Lett.* **112**, 116601 (2014).
- [23] T. Aktor, J. H. Garcia, S. Roche, A.-P. Jauho, and S. R. Power, Valley Hall effect and nonlocal resistance in locally gapped graphene, *Phys. Rev. B* **103**, 115406 (2021).
- [24] S. Roche, S. R. Power, B. K. Nikolić, J. H. García, and A.-P. Jauho, Have mysterious topological valley currents been observed in graphene superlattices? *J. Physics: Mater.* **5**, 021001 (2022).
- [25] Z. Wang, Y. B. Wang, J. Yin, E. Tóvári, Y. Yang, L. Lin, M. Holwill, J. Birkbeck, D. J. Perello, S. Xu, J. Zultak, R. V. Gorbachev, A. V. Kretinin, T. Taniguchi, K. Watanabe, S. V. Morozov, M. Anđelković, S. P. Milovanović, L. Covaci, F. M. Peeters *et al.*, Composite super-moiré lattices in double-aligned graphene heterostructures, *Sci. Adv.* **5**, eaay8897 (2019).
- [26] M. Yankowitz, J. Xue, D. Cormode, J. D. Sanchez-Yamagishi, K. Watanabe, T. Taniguchi, P. Jarillo-Herrero, P. Jacquod, and B. J. LeRoy, Emergence of superlattice Dirac points in graphene on hexagonal boron nitride, *Nat. Phys.* **8**, 382 (2012).
- [27] See Supplemental Material at <http://link.aps.org/supplemental/10.1103/PhysRevResearch.6.023212> for a step-by-step explanation of the sample fabrication (as shown in Ref. [49]), a detailed Raman characterization, quantum Hall characterization at low temperatures, and the estimation for the residual carrier density (see Refs. [50–52]), Ohmic and thermal contribution to  $R_{nl}$ , the detailed perturbation theory and linear response formalism for the orbital Hall effect (see Refs. [36,53–59]), and in-depth technical details of the nonlocal resistance simulations (see Refs. [60–62]).
- [28] L. Wang, Y. Gao, B. Wen, Z. Han, T. Taniguchi, K. Watanabe, M. Koshino, J. Hone, and C. R. Dean, Evidence for a fractional fractal quantum Hall effect in graphene superlattices, *Science* **350**, 1231 (2015).
- [29] N. R. Finney, M. Yankowitz, L. Muraleetharan, K. Watanabe, T. Taniguchi, C. R. Dean, and J. Hone, Tunable crystal symmetry in graphene-boron nitride heterostructures with coexisting moiré superlattices, *Nat. Nanotechnol.* **14**, 1029 (2019).
- [30] B. Hunt, J. D. Sanchez-Yamagishi, A. F. Young, M. Yankowitz, B. J. LeRoy, K. Watanabe, T. Taniguchi, P. Moon, M. Koshino, P. Jarillo-Herrero, and R. C. Ashoori, Massive Dirac fermions and Hofstadter butterfly in a van der Waals heterostructure, *Science* **340**, 1427 (2013).
- [31] A. Eckmann, J. Park, H. Yang, D. Elias, A. S. Mayorov, G. Yu, R. Jalil, K. S. Novoselov, R. V. Gorbachev, M. Lazzeri, A. K. Geim, and C. Casiraghi, Raman fingerprint of aligned graphene/h-BN superlattices, *Nano Lett.* **13**, 5242 (2013).
- [32] A. Marguerite, J. Birkbeck, A. Aharon-Steinberg, D. Halbertal, K. Bagani, I. Marcus, Y. Myasoedov, A. K. Geim, D. J. Perello, and E. Zeldov, Imaging work and dissipation in the quantum Hall state in graphene, *Nature (London)* **575**, 628 (2019).
- [33] Y. Yafet,  $g$  Factors and spin-lattice relaxation of conduction electrons, *Solid State Phys.* **14**, 1 (1963).
- [34] T. Thonhauser, D. Ceresoli, D. Vanderbilt, and R. Resta, Orbital magnetization in periodic insulators, *Phys. Rev. Lett.* **95**, 137205 (2005).
- [35] R. Bianco and R. Resta, Mapping topological order in coordinate space, *Phys. Rev. B* **84**, 241106(R) (2011).
- [36] T. Cai, S. A. Yang, X. Li, F. Zhang, J. Shi, W. Yao, and Q. Niu, Magnetic control of the valley degree of freedom of massive Dirac fermions with application to transition metal dichalcogenides, *Phys. Rev. B* **88**, 115140 (2013).
- [37] H. Zhou, C. Xiao, and Q. Niu, Valley-contrasting orbital magnetic moment induced negative magnetoresistance, *Phys. Rev. B* **100**, 041406(R) (2019).
- [38] J. Shi, P. Zhang, D. Xiao, and Q. Niu, Proper definition of spin current in spin-orbit coupled systems, *Phys. Rev. Lett.* **96**, 076604 (2006).
- [39] C. Xiao and Q. Niu, Conserved current of nonconserved quantities, *Phys. Rev. B* **104**, L241411 (2021).
- [40] C. W. Groth, M. Wimmer, A. R. Akhmerov, and X. Waintal, Kwant: A software package for quantum transport, *New J. Phys.* **16**, 063065 (2014).

- [41] T. B. Boykin, M. Luisier, G. Klimeck, X. Jiang, N. Kharche, Y. Zhou, and S. K. Nayak, Accurate six-band nearest-neighbor tight-binding model for the  $\pi$ -bands of bulk graphene and graphene nanoribbons, *J. Appl. Phys.* **109**, 104304 (2011).
- [42] B. Roy and K. Yang, Bilayer graphene with parallel magnetic field and twisting: Phases and phase transitions in a highly tunable Dirac system, *Phys. Rev. B* **88**, 241107(R) (2013).
- [43] Y. H. Kwan, S. A. Parameswaran, and S. L. Sondhi, Twisted bilayer graphene in a parallel magnetic field, *Phys. Rev. B* **101**, 205116 (2020).
- [44] S. S. Pershoguba and V. M. Yakovenko, Energy spectrum of graphene multilayers in a parallel magnetic field, *Phys. Rev. B* **82**, 205408 (2010).
- [45] Y. Asakawa, S. Masubuchi, N. Inoue, S. Morikawa, K. Watanabe, T. Taniguchi, and T. Machida, Intersubband Landau level couplings induced by in-plane magnetic fields in trilayer graphene, *Phys. Rev. Lett.* **119**, 186802 (2017).
- [46] M. M. Denner, J. L. Lado, and O. Zilberberg, Antichiral states in twisted graphene multilayers, *Phys. Rev. Res.* **2**, 043190 (2020).
- [47] W. Qin and A. H. MacDonald, In-plane critical magnetic fields in magic-angle twisted trilayer graphene, *Phys. Rev. Lett.* **127**, 097001 (2021).
- [48] L. F. Torres and S. O. Valenzuela, A valley of opportunities, *Phys. World* **34**, 43 (2021).
- [49] J. A. Delgado-Notario, W. Knap, V. Clericò, J. Salvador-Sánchez, J. Calvo-Gallego, T. Taniguchi, K. Watanabe, T. Otsuji, V. V. Popov, D. V. Fateev, E. Diez, J. E. Velázquez-Pérez, and Y. M. Meziani, Enhanced terahertz detection of multigate graphene nanostructures, *Nanophotonics* **11**, 519 (2022).
- [50] N. J. G. Couto, D. Costanzo, S. Engels, D.-K. Ki, K. Watanabe, T. Taniguchi, C. Stampfer, F. Guinea, and A. F. Morpurgo, Random strain fluctuations as dominant disorder source for high-quality on-substrate graphene devices, *Phys. Rev. X* **4**, 041019 (2014).
- [51] L. Wang, P. Makk, S. Zihlmann, A. Baumgartner, D. I. Indolese, K. Watanabe, T. Taniguchi, and C. Schönberger, Mobility enhancement in graphene by *in situ* reduction of random strain fluctuations, *Phys. Rev. Lett.* **124**, 157701 (2020).
- [52] D. Vaquero, V. Clericò, M. Schmitz, J. A. Delgado-Notario, A. Martín-Ramos, J. Salvador-Sánchez, C. S. A. Müller, K. Rubi, K. Watanabe, T. Taniguchi, B. Beschoten, C. Stampfer, E. Diez, M. I. Katsnelson, U. Zeitler, S. Wiedmann, and S. Pezzini, Phonon-mediated room-temperature quantum Hall transport in graphene, *Nat. Commun.* **14**, 318 (2023).
- [53] W. Kohn, Theory of Bloch electrons in a magnetic field: The effective Hamiltonian, *Phys. Rev.* **115**, 1460 (1959).
- [54] D. Faílde and D. Baldomir, Orbital dynamics in 2D topological and Chern insulators, *New J. Phys.* **23**, 113002 (2021).
- [55] M. Kindermann, B. Uchoa, and D. L. Miller, Zero-energy modes and gate-tunable gap in graphene on hexagonal boron nitride, *Phys. Rev. B* **86**, 115415 (2012).
- [56] Y. D. Lensky, J. C. W. Song, P. Samutpraphoot, and L. S. Levitov, Topological valley currents in gapped Dirac materials, *Phys. Rev. Lett.* **114**, 256601 (2015).
- [57] J. C. W. Song, P. Samutpraphoot, and L. S. Levitov, Topological Bloch bands in graphene superlattices, *Proc. Natl. Acad. Sci. USA* **112**, 10879 (2015).
- [58] T. P. Cysne, S. Bhowal, G. Vignale, and T. G. Rappoport, Orbital Hall effect in bilayer transition metal dichalcogenides: From the intra-atomic approximation to the Bloch states orbital magnetic moment approach, *Phys. Rev. B* **105**, 195421 (2022).
- [59] N. M. R. Peres, *Colloquium: The transport properties of graphene: An introduction*, *Rev. Mod. Phys.* **82**, 2673 (2010).
- [60] S. Konschuh, M. Gmitra, and J. Fabian, Tight-binding theory of the spin-orbit coupling in graphene, *Phys. Rev. B* **82**, 245412 (2010).
- [61] J. C. Slater and G. F. Koster, Simplified LCAO method for the periodic potential problem, *Phys. Rev.* **94**, 1498 (1954).
- [62] Y.-W. Son, M. L. Cohen, and S. G. Louie, Energy gaps in graphene nanoribbons, *Phys. Rev. Lett.* **97**, 216803 (2006).
- [63] <https://doi.org/10.54499/2022.07471.CEECIND/CP1718/CT0001>.